Article:

Zhai, J, Fairweather, M and Colombo, M (2020) Simulation of Microbubble Dynamics in Turbulent Channel Flows. Flow, Turbulence and Combustion, 105 (4). pp. 1303-1324. ISSN: 1386-6184

https://doi.org/10.1007/s10494-020-00136-y

Simulation of microbubble dynamics in turbulent channel flows

Jian Zhai* (ORCID: 0000-0002-1059-9534), Michael Fairweather, Marco Colombo

School of Chemical and Process Engineering

University of Leeds, Leeds LS2 9JT, United Kingdom

*Email addresses for correspondence: J. Zhai pmjzhai@leeds.ac.uk

Abstract

This work investigates microbubble dynamics in four-way (with coalescence) coupled microbubble-laden turbulent channel flows. Upward and downward flows of water at a shear Reynolds number of Re_τ = 150 are predicted using direct numerical simulation (DNS). Microbubbles, assumed to be non-deformable and spherical, are injected into the water flow and tracked using a Lagrangian approach. One-way and two-way coupled predictions were successfully compared against other available DNS-based results and used to demonstrate different trends in bubble preferential motion, with bubbles pushed by the lift force towards the wall in upflow and towards the centre of the channel in downflow. Four-way coupled simulations with bubble coalescence clearly demonstrate that the presence of the bubbles, and collisions between them, have a non-negligible effect on the fluid phase. Analysis of bubble collision behaviour highlights that binary collisions most frequently occur at very small approach angles and with low relative approach velocities. Once a collision is detected, the occurrence of bubble coalescence is evaluated, with special attention given to the performance of different bubble coalescence models. The film drainage model returns a 100% coalescence efficiency, while on the other hand the energy model returns a 0% coalescence efficiency, with this large discrepancy requiring further investigation and model development. The knowledge gained from the present results on the mechanisms that underpin bubble collisions is of value to the further development of more advanced coalescence closure models.

Keywords: Direct numerical simulation, microbubbles, turbulence modulation, bubble coalescence

1 Introduction

Dispersed bubbly flows consist of a population of gas bubbles dispersed in a liquid continuum. Bubbly flows of different kinds are found in a number of natural phenomena and are also widely used in engineering applications [1]. In nuclear power plants cooled by water, bubbly flows are commonly encountered when boiling occurs and a large number of bubbles are generated on the heated walls [2]. Also, bubble columns are widely used in chemical and petrochemical reaction units, since they remove the need for moving parts and have good hydrodynamic and mass/heat transfer characteristics, even with large liquid holdup [3,4]. However, bubbly flows hydrodynamics is complex and one of the major complexities derives from bubble interactions with neighbouring bubbles and with the usually turbulent fluid flow. When the gas void fraction increases above ~ 3%, bubble-bubble interactions are no longer negligible [5]. These interactions promote bubble coalescence, with turbulence also leading to bubble break-up, and these phenomena impact the bubble size distribution within the flow and make the accurate prediction of bubbly flows in practical applications particularly challenging.

With the development of high performance computing (HPC) platforms in recent decades, numerical simulations are now capable of resolving fluid dynamic details that are difficult to capture even with the most advanced experimental techniques. Over the years, numerous advanced computational fluid dynamic methods have been developed for predicting turbulent bubbly flows. Among these approaches, direct numerical simulation (DNS) resolves all the length and time scales in the flow down to the Kolmogorov scale, and has been increasingly used to advance the understanding of complex flow phenomena across the length scales down to the smallest scales. The knowledge generated through DNS studies currently often underpins, together with experimental data, the further improvement of closure relations employed in more macroscopic treatments, such as the Eulerian-Eulerian multi-fluid model [6]. In the context of bubbly flows, DNS has started to be applied only relatively recently, once the growth of HPC made it computationally affordable [7]. In this paper, DNS is used to advance the current knowledge of some aspects of the fluid dynamics of two-phase bubbly flows.

With knowledge of the flow field obtained using DNS, different methodologies can be employed for the computation of the flow of the dispersed bubbles, such as Lagrangian or interface tracking techniques. Of these, coupled Eulerian-Lagrangian approaches treat the continuous phase in an Eulerian framework and the motion of individual or groups of bubbles by solving Newton's second law of motion, accounting for all the forces acting on each bubble.

By incorporating bubble-fluid and bubble-bubble interactions (e.g. bubble collisions, coalescence and break-up), the method provides a means to simulate phase interaction with a much higher spatial resolution with respect to other methods such as Eulerian-Eulerian approaches [8]. Over the decades, Eulerian-Lagrangian approaches have successfully been applied to the simulation of microbubble behaviour in turbulent flows [9-13]. In this work, an Eulerian-Lagrangian model, with DNS used to predict the liquid phase flow field, is developed and applied to bubbly flows in a vertical channel.

Of interest in this study is the behaviour of microbubbles, these being bubbles with a diameter in the range 1 ~ 1000 μm. This size range is relevant in many engineering applications, such as the treatment of waste water and sewage, where microbubbles help to separate particulates from potable water due to their high surface area to volume ratio [14]. The flow of microbubbles in channels has been investigated numerically many times over the last few decades [9,15-21,13,22], but available studies mainly focus only on aspects such as the modulation of turbulence by microbubbles, the reduction of turbulent skin friction, and the lift force effect on the bubble spatial distribution. However, in real life gas-liquid processes, bubbles constantly collide with each other. Depending on the size, velocity and interfacial chemistry, the bubbles may break-up or coalescence [23], changing the total number of bubbles in the flow and the bubble size distribution. These phenomena impact not only the fluid flow and turbulence field, but sometimes more importantly heat and mass transfer processes through the available interfacial area.

Experimental observations in the literature [24-27] have helped to clarify microbubble dynamics and the effect of bubbles on the fluid flow, as well as some characteristics of their coalescence behaviour. For example, Park et al. [25] demonstrated that microbubbles in a turbulent boundary layer favour accumulation in the low-speed streaks close to the viscous sublayer, and form hairpin shaped clouds in the buffer region. These results help to clarify how microbubble clouds form in the turbulent boundary layer. However, microbubble coalescence was not observed in their study, even in the clouds. The authors attributed this to the rigidity of the microbubbles due to their high surface tension and local repulsion at the water/microbubble surface. The study was, however, limited to a bubble volume fraction of α < 0.01%. At higher volume fractions of $\alpha = 0.10\%$, Yonemoto et al. [26] observed microbubble coalescence even in purified water. They noted that microbubbles can slide along the surface of another bubble, bouncing off after, although in other cases, the bubbles immediately coalesced after contact, or after a certain amount of interaction time. In view of this, although progress has been made recently, a comprehensive understanding of microbubble collision and coalescence behaviour is still to be achieved.

In the literature, three methods are employed to predict the coalescence probability of interacting bubbles [28]: the film drainage model [29,30], the energy model [31] and the critical approach velocity model [32]. In the commonly used film drainage model, when two bubbles approach and touch one another, a liquid film is trapped between their interfaces. If the bubbles remain in contact for enough time to allow the film to drain away to the critical rupture thickness, bubble coalescence occurs. Otherwise, the two bubbles bounce off each other. Clearly, this is a complex process to model and is greatly affected by the interface properties. Most numerical studies [23,33,34] of microbubble coalescence have focused on surfactant-laden flows and it is well known that tiny amounts of contaminants or surfactants can drastically modify the air-water interface behaviour [35]. Experimental results reveal that clean air bubbles coalesce within milliseconds, much faster than when contaminants are present. To the authors' knowledge, most research to date has concerned the use of large eddy simulation to study microbubble flows under four-way coupling with coalescence, e.g. [36,37], with DNS-based investigations of clean bubbles notable scarce.

In this paper, microbubble-laden channel flows are predicted using DNS and a Lagrangian particle tracking approach. In line with previous work [17, 22], microbubbles with diameters 110 μm, 220 μm and 330 μm, assumed to be non-deformable and spherical, are injected and allowed to collide and coalesce. The predicted bubble dynamics and interactions in the turbulent flow are evaluated, and the impact of the fluid turbulence on bubble collision, coalescence and the bubble size evolution are considered.

Section 2 presents the computational approaches employed, specifically the DNS and Lagrangian particle tracking models. In Section 3, model results are initially validated against literature results for single-phase, one-way and two-way coupled flows. Subsequently, the model is extended to four-way coupling with the addition of specific models to detect bubble collision and evaluate coalescence probability. The capabilities of the four-way coupled model are evaluated in upward and downward channel flows of water at $Re_\tau = 150$, and results for bubble collision and coalescence efficiency analysed. It should be noted that previous work [33] has indicated that bubble break-up is negligible in low Reynolds number channel flows of the order of that studied in this work, and hence it is not considered further in this work. A summary of the key findings of the work and general conclusions are provided in Section 4.

2 Numerical Approach

In this section, the numerical model employed for the DNS of turbulent bubbly flow is described. In Section 2.1, the governing equations for the fluid phase are presented, followed by the description of the Nek5000 fluid flow solver used in this work. The Lagrangian particle tracking routine, developed and interfaced with the Nek5000 code, is introduced in Section 2.2. Finally, in Section 2.3, discretization of the computational domain and the numerical setup are presented.

2.1 Fluid phase

The high order spectral element Nek5000 code [38] was used to solve for the turbulent fluid flow. DNS codes rely on accurate and efficient solution algorithms that have low numerical dissipation and fine time and space discretization to solve for all the turbulent scales in the flow. Nek5000 is well known for its spectral accuracy, favourable dispersion properties and efficient parallelization [39]. Nek5000 is a Legendre polynomial-based spectral element code and was used to solve the continuity and momentum conservation equations for the fluid phase flow, written in non-dimensional form:

$$\nabla \cdot \boldsymbol{u}^* = 0 \tag{1}$$

$$\frac{\partial \boldsymbol{u}^*}{\partial t^*} + (\boldsymbol{u}^* \cdot \nabla)\boldsymbol{u}^* = -\nabla p^* + \frac{1}{Re_b}\nabla^2 \boldsymbol{u}^* + \boldsymbol{f}_i^* \tag{2}$$

Here, $\boldsymbol{u}^*$ is the velocity vector of the fluid flow field, and p^* is the pressure. Re_b is the bulk flow Reynolds number ($Re_b = U_b\,\delta\,/\,\nu$, with fluid kinematic viscosity ν). $\boldsymbol{f}_i^*$ is an arbitrary forcing term that incorporates the imposed pressure gradient used to drive the single-phase flow and feedback from the bubbles to the fluid phase (two-way coupling). All the parameters are normalized by bulk quantities, using the channel half-height δ as the reference length scale and the bulk velocity U_b as the reference velocity scale, which gives the reference time scale as δ / U_b. Further details of the code can be found in [35]. The use of Eqs. (1) and (2), neglecting effects due to local variations of the bubble volume fraction, is only valid for volume fractions < 0.1% [5]. For higher volume fractions, according to Ferrante and Elghobashi [21], the presence of a local positive divergence of the fluid velocity would affect the accuracy of the method. In the present work, and in view of the results given below, this is only likely to have any effect in the viscous sublayer in upflow.

2.2 Bubble phase

In order to model the transport of the dispersed phase, a Lagrangian bubble tracking routine was developed and interfaced with Nek5000. Each bubble is assumed spherical and represented by a Lagrangian point. The movement of each bubble is tracked by solving the non-dimensional form of Newton's equation of motion, using a fourth-order Runge–Kutta scheme, with a timestep equal to that of the fluid flow solver. Forces acting on the bubble are drag, lift, virtual mass, pressure gradient, gravity and buoyancy:

$$\rho_b^* \frac{d\boldsymbol{u}_b^*}{dt^*} = \frac{3C_\mathrm{D}}{4d_b^*}\left|\boldsymbol{u}_f^* - \boldsymbol{u}_b^*\right|\left(\boldsymbol{u}_f^* - \boldsymbol{u}_b^*\right) + (1-\rho_b^*)\boldsymbol{g}^* + C_\mathrm{VM}\left(\frac{D\boldsymbol{u}_f^*}{Dt^*} - \frac{d\boldsymbol{u}_b^*}{dt^*}\right) + \frac{D\boldsymbol{u}_f^*}{Dt^*} + C_\mathrm{L}\left(\boldsymbol{u}_f^* - \boldsymbol{u}_b^*\right) \times \boldsymbol{\omega}_f^* \tag{3}$$

where ρ_b^* is the non-dimensional bubble density, $\boldsymbol{u}_f^*$ and $\boldsymbol{u}_b^*$ are the non-dimensional fluid and bubble velocity vectors, C_D is the drag coefficient, C_VM the virtual mass coefficient and C_L is the lift coefficient. The non-dimensional gravitational acceleration $\boldsymbol{g}^*$ is only set in the streamwise direction, given the Froude number Fr. $\boldsymbol{\omega}_f^*$ the fluid vorticity at bubble position and is given as $\boldsymbol{\omega}_f^* = \nabla \times \boldsymbol{u}_f^*$. The bubble position is obtained from:

$$\frac{d\boldsymbol{x}_b^*}{dt^*} = \boldsymbol{u}_b^* \tag{4}$$

where $\boldsymbol{x}_b^*$ represents the coordinates of the bubble position.

The first term on the right-hand side of Eq. (3) is the drag force, which is the force exerted by the continuous phase that opposes bubble movement. For rising bubbles at steady-state, the drag force is balanced by the buoyancy force and determines the relative velocity between the bubble and the continuous phase fluid. The drag coefficient C_D is obtained from the model of Schiller and Naumann [40], which provides a non-linear correction to the Stokesian drag force. The second term on the right-hand side of Eq. (3) combines the effects of gravity and buoyancy forces. The added-mass force characterizes the force acting on the bubbles because of the fluid displaced during bubble motion. In Eq. (3), this is associated with the substantial derivative of the fluid velocity at the bubble position and the total derivative of the bubble velocity. The virtual mass coefficient C_VM is set to 0.5, which is a reasonable assumption for spherical bubbles [41]. The pressure gradient force arises because of the presence of pressure gradients in the fluid phase and the expression used for this force is that given by Maxey and Riley [42]. The lift force is the final term and accounts for the force acting on the bubble in the direction perpendicular to its motion due to the presence of shear in the fluid flow, This lift force, as will be shown in the results section, drives the lateral movement of the bubbles and can be calculated using:

$$\boldsymbol{F}_{\mathrm{L}} = C_{\mathrm{L}} \rho_f V \left(\boldsymbol{u}_f - \boldsymbol{u}_b \right) \times \boldsymbol{\omega}_f \tag{5}$$

The lift coefficient C_{L} is taken from Legendre and Magnaudet [43], which combines large and small Reynolds number formulations. All the models used are summarized in Table 1.

Table 1. Equations for force coefficients.

Coefficient	Formula	Source
C_{D}	$C_{\mathrm{D}} = \frac{24}{Re_B}(1 + 0.15 Re_B^{0.687})$ $Re_B = \frac{\lvert u_f - u_b \rvert d_b}{\nu}$	Schiller and Naumann [40]
C_{VM}	0.5	Brennen [41]
C_{L}	$C_{\mathrm{L}} = \sqrt{[C_{\mathrm{L}}^{low\ Re}(Re_B, Sr_B)]^2 + \left[C_{\mathrm{L}}^{high\ Re}(Re_B)\right]^2}$ $C_{\mathrm{L}}^{low\ Re}(Re_B, Sr_B) = \frac{6}{\pi^2 (Re_B Sr_B)^{0.5}} \left[\frac{2.255}{(1+0.2\zeta^{-2})^{1.5}}\right]$ $C_{\mathrm{L}}^{high\ Re}(Re_B) = \frac{1}{2}\frac{Re_B + 16}{Re_B + 29}$ $Sr_B = \frac{\lvert \omega_b \rvert d_b}{2 \lvert u_f - u_b \rvert},\ \zeta = \left(\frac{Sr_B}{Re_B}\right)^{0.5}$	Legendre and Magnaudet [43]
Fr	$Fr = \frac{u_\tau^2}{g\delta}$	-

Here, Sr_B is the non-dimensional shear rate, and Re_B is the bubble Reynolds number.

Two-way coupling was achieved by including feedback from each bubble to the fluid phase via the $\boldsymbol{f}_i^*$ term in the momentum conservation equation (Eq. (2)).

When the bubble concentration is sufficiently high, the number of bubble collisions increases significantly. The effect of these on the fluid dynamics of the flow can no longer be neglected, and it is necessary to move to four-way coupled simulations. In this work, only binary collisions between bubbles were considered and these were modelled using a hard sphere collision approach. When two bubbles collide, there are two possible outcomes, i.e. the two bubbles merge and coalesce or they bounce off each other after the collision. Numerous models are available to determine whether the bubbles coalesce after collision. These have been recently summarized in the comprehensive work of Liao and Lucas [28]. In the present work, the film drainage model proposed by Prince and Blanch [44] was adopted, coupled to the contact time models of Sommerfeld et al. [45] and Kamp et al. [46]. In addition, an energy model [47] for the coalescence process was also evaluated.

According to the film drainage model, when two bubbles collide a thin liquid film remains trapped between them [48,49]. Coalescence only happens if the interaction between the bubbles lasts long enough to allow the liquid to drain and the film to thin down to a thickness at which film rupture occurs. In the model, this happens only when the bubble contact time $t_{contact}$ is greater than the film drainage time $t_{drainage}$. The contact time was first modelled according to Sommerfeld et al. [45]:

$$t_{contact} = \frac{C_c r_{eq}}{u_n} \tag{6}$$

Here, r_{eq} is the equivalent bubble radius of two colliding unequal sized bubbles of radius r_1 and r_2. C_c is a constant that determines the deformation distance as a fraction of the effective bubble radius and u_n is the normal component of the relative impact velocity.The drainage time was taken from Prince and Blanch [44]:

$$t_{drainage} = \sqrt{\frac{{r_{eq}}^3 \rho_C}{16\sigma}} ln\left(\frac{h_0}{h_f}\right) \tag{7}$$

where σ is the surface tension and ρ_c the density of the continuous fluid phase. For an air-water system, the initial film thickness h_0 and the final thickness before rupture h_f were taken to be 10^{-4} m and 10^{-8} m, respectively [41]. The contact time from Kamp et al. [46] was also tested. In this model, the contact time is obtained from a balance between the increasing surface free energy and the corresponding reduction in the kinetic energy of the system during collision:

$$t_{contact} = \frac{\pi}{4}\left(\frac{8\rho_c C_{VM} r_{eq}^3}{3\sigma}\right)^{1/2} \tag{8}$$

In contrast to the film drainage model, a different approach is followed in the energy model developed by Howarth [31]. In this model, coalescence depends on the impact of the colliding bubbles, i.e. the relative velocity of two colliding bubbles should be larger than a critical value for coalescence to occur. Based on this, Sovová [47] proposed the energetic collision model, in which coalescence occurs if the kinetic collision energy E_{kin} exceeds the surface energy E_s:

$$E_s = 4\sigma\left(\frac{\pi}{6}\right)^{2/3}(r_1^2 + r_2^2) \tag{9}$$

$$E_{kin} = \frac{2\pi}{3}\rho_g u_{rel}^2 \frac{r_1^3 r_2^3}{r_1^3 + r_2^3} \tag{10}$$

The new bubble's radius after coalescence was calculated on a volume balance:

$$r_{new} = ({r_1}^3 + {r_2}^3)^{1/2} \tag{11}$$

2.3 Flow configuration

The flow domain studied is a vertical channel, modelled with two parallel walls. The size of the computational domain is $14\delta \times 2\delta \times 6\delta$, and it is discretized into 27 × 18 × 23 elements and 3.8 M Gauss-Lobatto-Legendre (GLL) grid-points, using 7th order spectral elements. The geometrical dimensions are comparable to those used by other authors studying turbulent bubble-laden channel flows [50-52]. The grid resolution is also comparable to, or higher than, other available literature studies of the same flow condition [17,22]. Streamwise, wall-normal and spanwise directions are denoted by x, y and z, respectively, and periodic conditions were assumed in both the streamwise and spanwise directions. The elements were uniformly distributed in the streamwise and spanwise directions, corresponding to grid spacings in the x direction of $\Delta x^+ = 11.1$ and in z direction of $\Delta z^+ = 5.6$ (in wall units). To capture the small-scale vortices in the near-wall region, elements were clustered in the wall-normal direction, so that on average the largest grid spacing equalled $\Delta {y^+}_c = 6.5$ in the channel centre, with the smallest equal to $\Delta {y^+}_w = 0.6$ in the near-wall region. The no-slip condition was imposed at the walls and the flow was driven by an imposed pressure gradient in the streamwise direction, determined from the desired Reynolds number. In this case, the fluid is water with density of 1000 $\text{kg}\cdot\text{m}^{-3}$ and kinematic viscosity of 10^{-6} $\text{m}^2\cdot\text{s}^{-1}$. The non-dimensional channel height δ is equal to 0.02 m and the shear velocity is 7.5×10^{-3} $\text{m}\cdot\text{s}^{-1}$, based on a shear Reynolds number $Re_\tau = 150$ which corresponds to a bulk mean velocity of 0.113 $\text{m}\cdot\text{s}^{-1}$.

Initially, a single-phase flow at $Re_\tau = 150$ was simulated until a statistically steady-state was reached. Then, a total of 181,340 and 22,659 bubbles of diameters $d_b = 110$ μm and 220 μm, respectively, were injected for the one-way and two-way coupled cases considered for model validation. These numbers of bubbles correspond to a void fraction of 0.01% which is low enough for bubble-bubble interactions to be neglected. The bubbles were injected with a random spatial distribution in the fully developed turbulent channel flow, with the initial bubble velocities matching those of the fluid at the bubble centre. When a bubble reached a periodic boundary, it was re-injected at the corresponding boundary on the other side of the channel, keeping the average void fraction of the bubbles constant. Both upflow and downflow cases were studied and the results validated against the DNS-based simulations of Giusti et al. [22]

and Molin et al. [17]. For the four-way coupled cases, the number of 110 μm diameter bubbles was increased to 1,928,513. This number of bubbles was used to obtain a void fraction of 0.1%, necessary to record a significant number of bubble collisions. These simulations were also performed with 71,426 330 μm diameter bubbles giving the same void fraction. The nondimensional Eotvos number (*Eo*) can be introduced to describe bubble deformability:

$$Eo = \frac{(\rho_c - \rho_b) d_b^2 g}{\sigma} \tag{12}$$

The Eotvos number is proportional to the buoyancy force divided by the surface tension force. In this paper, the surface tension is assumed to be 0.0728 $\mathrm{N \cdot m^{-1}}$, and the densities of the fluid and bubbles are 1000 $\mathrm{kg \cdot m^{-3}}$ and 1.3 $\mathrm{kg \cdot m^{-3}}$, respectively, leading to $Eo \approx 1.63 \times 10^{-3}$ for 110 μm diameter bubbles, and $Eo \approx 6.51 \times 10^{-3}$ and 1.46×10^{-2} for 220 and 330 μm diameter bubbles. Considering that $Eo < 0.2$ for all bubble sizes, and the level of turbulence considered in this study, it is reasonable to assume that each microbubble is non-deformable and spherical [53].

3 Results and Discussion

3.1 Model validation

The instantaneous single-phase velocity field is displayed in **Fig. 1** for the $Re_\tau = 150$ flow, together with the GLL grid-points. The streamwise velocity is seen to be at a maximum in the centre of the channel and decreases to a minimum towards the walls due to the non-slip boundary conditions applied there. Validation of these results was obtained by comparison with the DNS predictions of Molin et al. [17]. Time- and space-averaged predictions, normalized by shear variables (the shear velocity u_τ is used as the reference velocity scale rather than the bulk velocity U_b), are compared in **Fig. 2**. The present results for the single-phase flow are plotted as solid lines, while the circles correspond to the predictions of Molin et al. [17]. Excellent agreement is obtained for the mean streamwise velocity in **Fig. 2(a)** and the root-mean-square (rms) of the velocity fluctuations in **Fig. 2(b)**. Predictions of the $u_x'^{+} u_y'^{+}$ shear stress from the present computations are also included in the latter, although similar values were not provided by Molin et al. [17]. Although not shown, comparable agreement to that shown in **Fig. 2** was also obtained for a $Re_\tau = 395$ single-phase channel flow considered by Molin et al. [17].

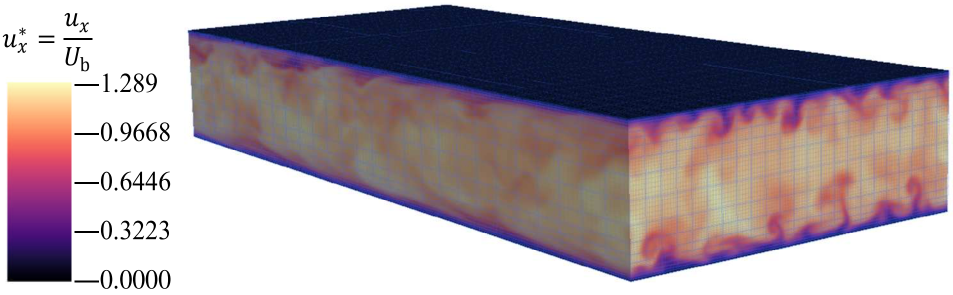

Figure 1. Computational mesh and non-dimensional instantaneous streamwise velocity in the single-phase channel flow at $Re_\tau = 150$.

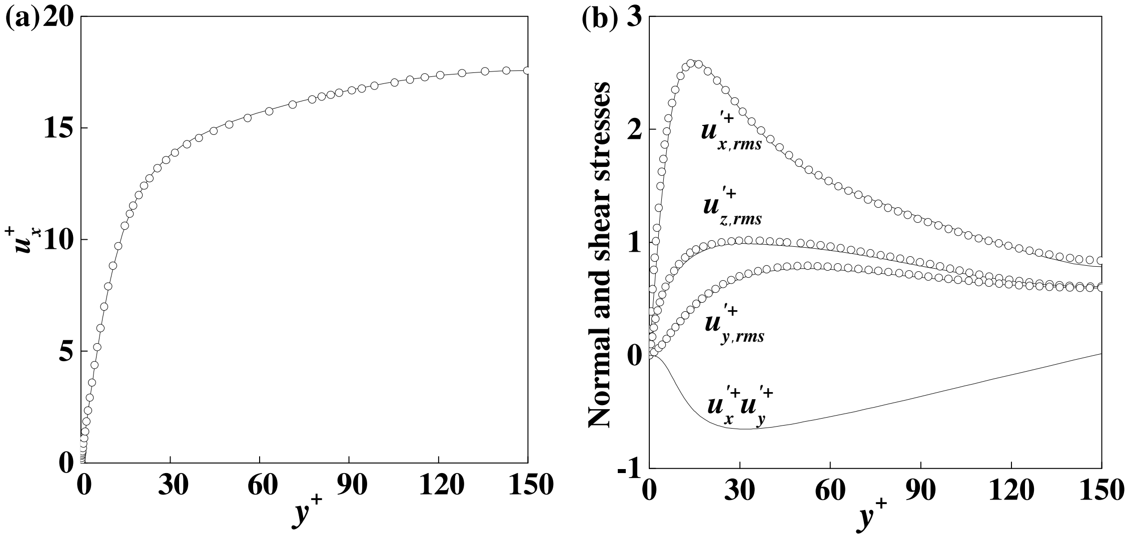

Figure 2. Comparisons for single-phase fluid flow at $Re_\tau = 150$: — present work; ○ Molin et al. [17]. (a) Mean streamwise fluid velocity (u_x^+); (b) wall-normal ($u'^+_{y,rms}$), spanwise ($u'^+_{z,rms}$) and streamwise ($u'^+_{x,rms}$) rms of velocity fluctuations, and shear stress ($u'^+_x u'^+_y$).

Turning to the simulations of microbubble-laden flows, microbubbles of diameters $d_b = 110$ μm and 220 μm were injected into the statistically steady single-phase flow solution at $Re_\tau = 150$. Results for the bubble distribution in the one-way coupled upflow with $d_b = 220$ μm bubbles are presented in **Fig. 3**. The lateral movement of bubbles is driven by the lift force (Eq.(5)), which pushes spherical bubbles, due to the asymmetrical fluid circulation around the bubble in a shear flow, towards the side of higher relative velocity [54]. In upflow, since the bubbles travel faster than the liquid, the higher relative velocity is found on the side of the bubble towards the wall, where the fluid is slower (**Fig. 3(a)**). In contrast, in downflow (not shown), the bubble is slower than the liquid and, accordingly, the highest relative is found on the side towards the centre of the channel, where the fluid velocity is higher. **Fig. 3(b)** shows the bubble distribution close to the wall in the same upward channel flow, superimposed on contours of the fluid velocity field. Clearly, the bubbles preferentially concentrate in the well-known regions of low fluid velocity (or low speed streaks) near the walls, caused by quasi-streamwise vortices, i.e. long, thin tubes of vorticity, that are orientated mainly in the streamwise direction.

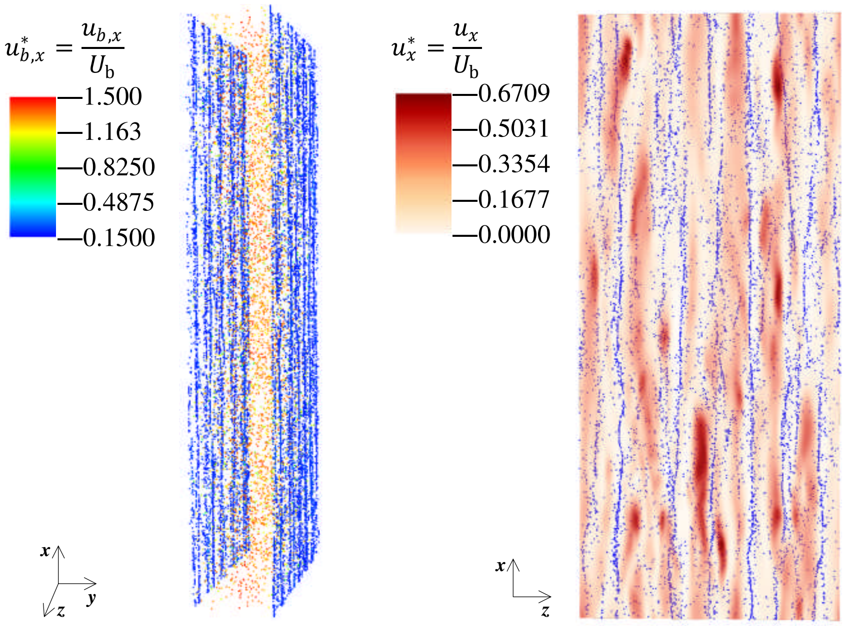

(a) (b)

Figure 3. Instantaneous bubble distribution in upflow at Re_τ = 150 for d_b = 220 μm bubbles: (a) distribution with contour levels of bubble streamwise velocity in the whole channel; and (b) distribution in a thin slice of the viscous sublayer with contour levels of fluid streamwise velocity.

Two-way coupled simulations, where the effects of bubbles on the carrier fluid are accounted for, were also validated against the Molin et al. [17] database used for the single-phase flow simulation. For the validation, the pressure gradient was modified in agreement with that used by Molin et al. [17] to include the reduced gravitational gain or loss consequence of the lighter mixture. As discussed in Molin et al. [17], this leads to a higher/lower wall shear, and mean velocity, in the upward/downward two-way coupled flows with respect to the single-phase flow. For the downward flow, the comparison with Molin et al. [17] is presented in **Fig. 4**. Bubbles travel slower than the fluid in this case and, although some differences are found in the shape of the predicted streamwise mean bubble velocity, this and the rms values given in **Fig. 4(b)** are in acceptable agreement. The same results for the upflow case are provided in **Fig. 5**. Here, the bubbles travel faster than the fluid, but the difference in the mean streamwise bubble velocity with respect to Molin et al.’s [17] results is more marked than in the downflow case, but with generally good agreement for rms values. This can be explained by the fact that, in the present simulations, the pressure gradient was fixed to exactly match that estimated in Molin et al.’s [17] study after the injection of the bubbles. In the latter study, however, it is shown that the real wall shear in the simulation does not reach this estimated value but remains lower, causing the fluid, and the bubbles, to travel slower with respect to the present simulation, where the estimated wall shear is effectively reached. Additionally, the present computations used 3.8 M grid-points compared to the 2.1 M nodes used by Molin et al. [17].

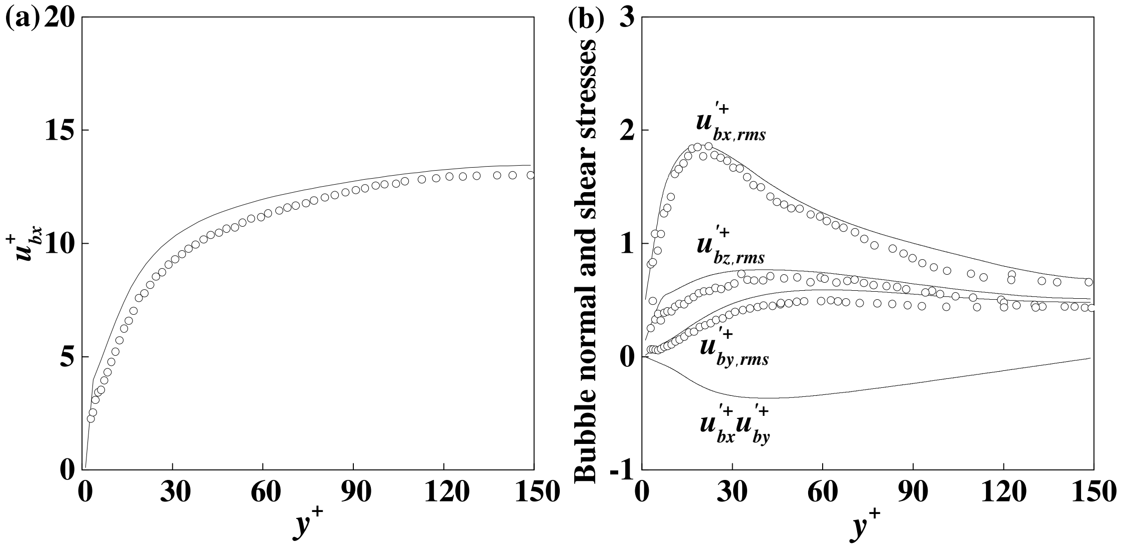

Figure 4. Comparison of bubble velocity statistics for two-way coupled downflow at $Re_\tau = 150$ with $d_b = 110$ µm: — present work; ○ Molin et al. [17]. (a) Mean streamwise bubble velocity (u^+_{bx}); (b) wall-normal ($u'^+_{by,rms}$), spanwise ($u'^+_{bz,rms}$) and streamwise ($u'^+_{bx,rms}$) rms of bubble velocity fluctuations, and shear stress ($u'^+_{bx}u'^+_{by}$).

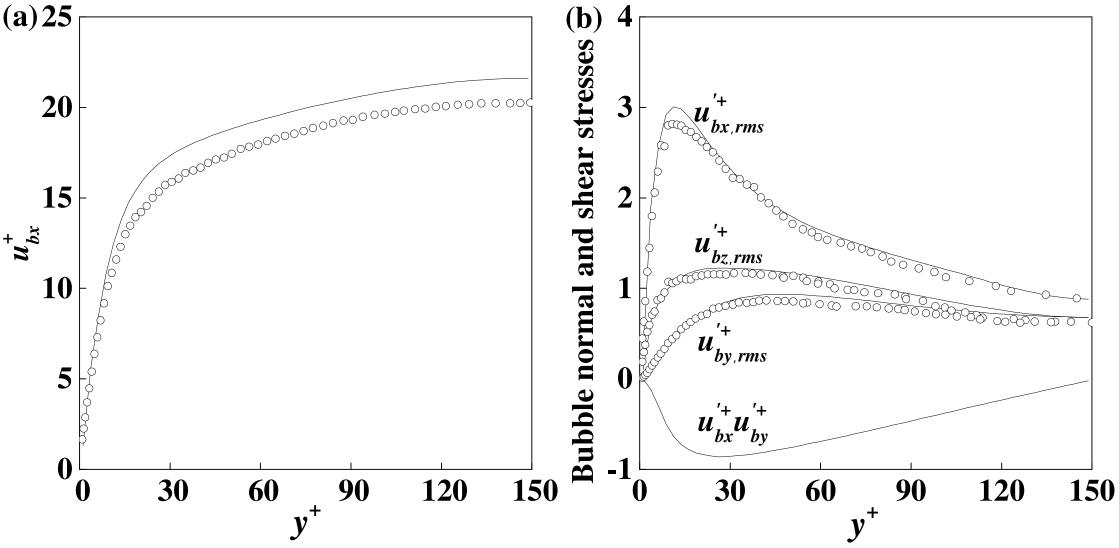

Figure 5. Comparison of bubble velocity statistics for two-way coupled upflow at $Re_\tau = 150$ with $d_b = 110$ μm: — present work; ○ Molin et al. [17]. (a) Mean streamwise bubble velocity (u^{+}_{bx}); (b) wall-normal ($u'^{+}_{by,rms}$), spanwise ($u'^{+}_{bz,rms}$) and streamwise ($u'^{+}_{bx,rms}$) rms of bubble velocity fluctuations, and shear stress ($u'^{+}_{bx}u'^{+}_{by}$).

Although not shown, good agreement was found in comparisons with the continuous and dispersed phase DNS-based results of Giusti et al. [23] for $Re_\tau = 150$ upward and downward channel flows containing $d_b = 220$ μm bubbles that were one-way coupled to the flow.

3.2 Four-way coupled flows with d_b = 110 μm bubbles

After validation, the four-way coupled model was applied to upward and downward flows at $Re_\tau = 150$ with $d_b = 110$ μm bubbles, and a void fraction of 0.1%. The bubble mean streamwise velocity profiles, and normal and shear stresses, for both upflow and downflow are compared in **Fig. 6**. **Fig. 6(a)** shows that, as expected, bubbles travel faster in upflow than in downflow. Similar levels of bubble normal and shear stresses are found in the two flows (**Fig. 6(b)**), except for the peaks in the near-wall region where the streamwise normal stress and the shear stress are greater in upflow. This follows from the tendency of bubbles to enhance the fluid flow turbulence in upflow and suppress it in downflow [17,55]. Only in the immediate vicinity of the wall do rms values in downflow become higher, but this is simply a consequence of the small number of bubbles in this region that prevented statistically meaningful averaging. Therefore, results very close to the wall are not shown for the downflow case.

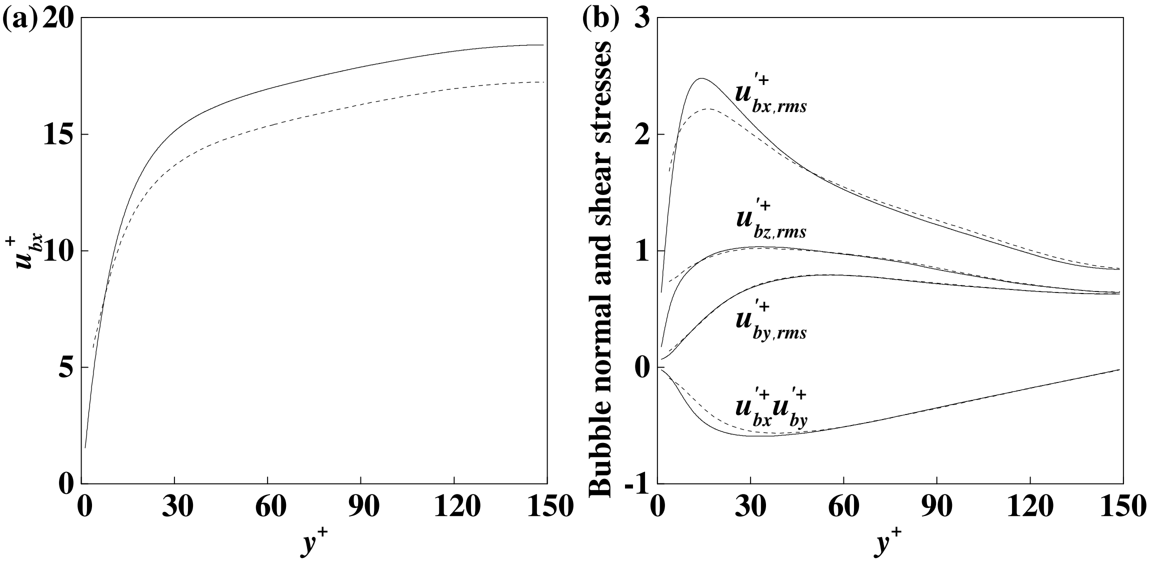

Figure 6. Bubble velocity statistics for four-way coupled (—) upflow and (- - -) downflow at Re_τ = 150 with d_b = 110 μm. (a) Mean streamwise velocity (u^+_{bx}); (b) wall-normal ($u'^+_{by,rms}$), spanwise ($u'^+_{bz,rms}$) and streamwise ($u'^+_{bx,rms}$) rms of bubble velocity fluctuations, and shear stress ($u'^+_{bx}u'^+_{by}$).

This effect is explained by the results given in **Fig. 7**, where the bubble number density, normalized by its initial value, is plotted as a function of the distance from the wall. Under the effect of the lift force, more bubbles travel towards the wall in upflow, with the bubble concentration peaking at the wall. Conversely, in downflow, the same lift force pushes the slower bubbles towards the centre of the channel and a bubble depleted region is formed in the near-wall region.

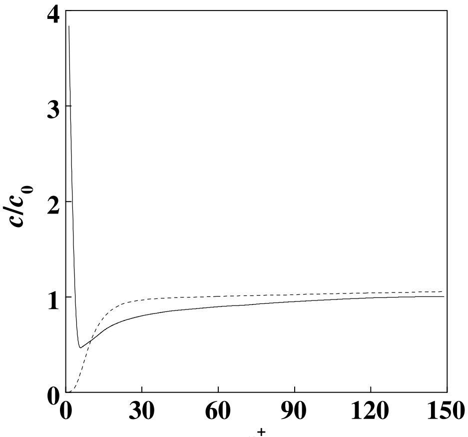

Figure 7. Four-way coupled bubble number density profiles normalized by the initial bubble concentration in (—) upflow and (- - -) downflow at Re_τ = 150 with d_b = 110 μm.

The Lagrangian bubble tracking technique employed allowed the systematic tracking of all bubble collisions and, for each of these, the velocity of the colliding bubbles and the collision angles. These quantities are of particular interest since detailed quantitative information on these parameters is generally not available, with many aspects of bubble collision and coalescence in turbulent flows still poorly understood. In **Fig. 8**, the probability density function (PDF) of relative bubble collision velocities in the streamwise direction are plotted in different regions of the channel (namely the viscous sublayer, buffer layer, log-law region, and bulk flow region) for the downflow case. In **Fig. 9**, similar information is provided for the bubble collision angles. The relative velocities, and angles, are always very small. Thus, despite the turbulent nature of the flow (albeit at low levels given the flow Reynolds number), these results indicate that most collisions involve bubbles colliding at low relative velocities whilst moving in only slightly different directions. It is notable that the largest collision angles, and velocities, are found in the viscous sublayer region, where the largest mean flow velocity gradients occur, but the lowest turbulence levels are found. At the shear Reynolds number considered, therefore, shear-induced collisions still play a significant role and turbulence affects bubble motion mainly in the streamwise direction, resulting in collisions that are almost rectilinear and with streamwise-only relative velocities.

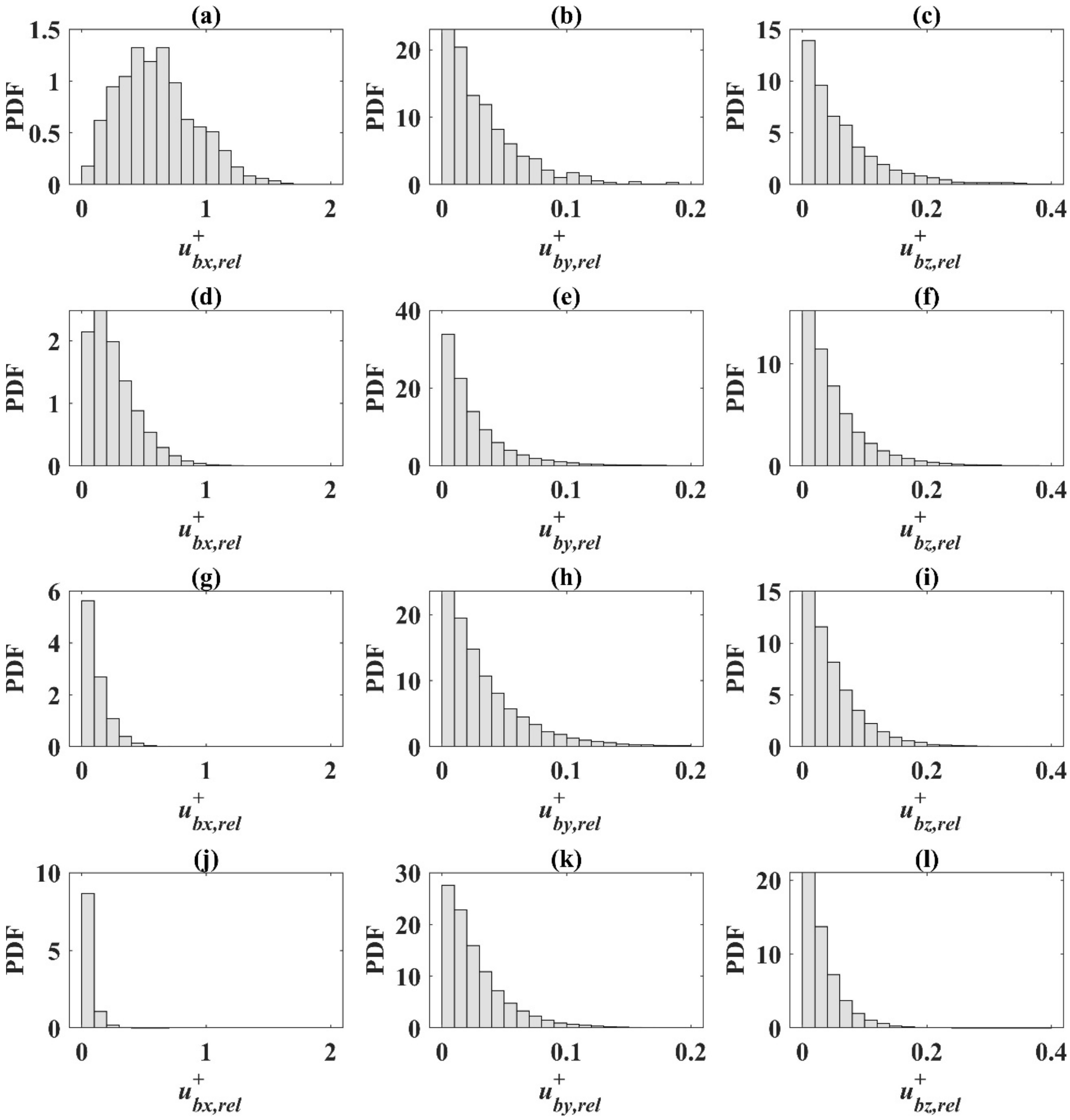

Figure 8. PDF of relative bubble collision velocities in the streamwise (x), wall-normal (y) and spanwise (z) directions in different regions of the channel in downflow at $Re_\tau = 150$ with d_b = 110 µm. (a), (b), (c) Viscous sublayer; (d), (e), (f) buffer layer; (g), (h), (i) log-law region; (j), (k), (l) bulk flow region.

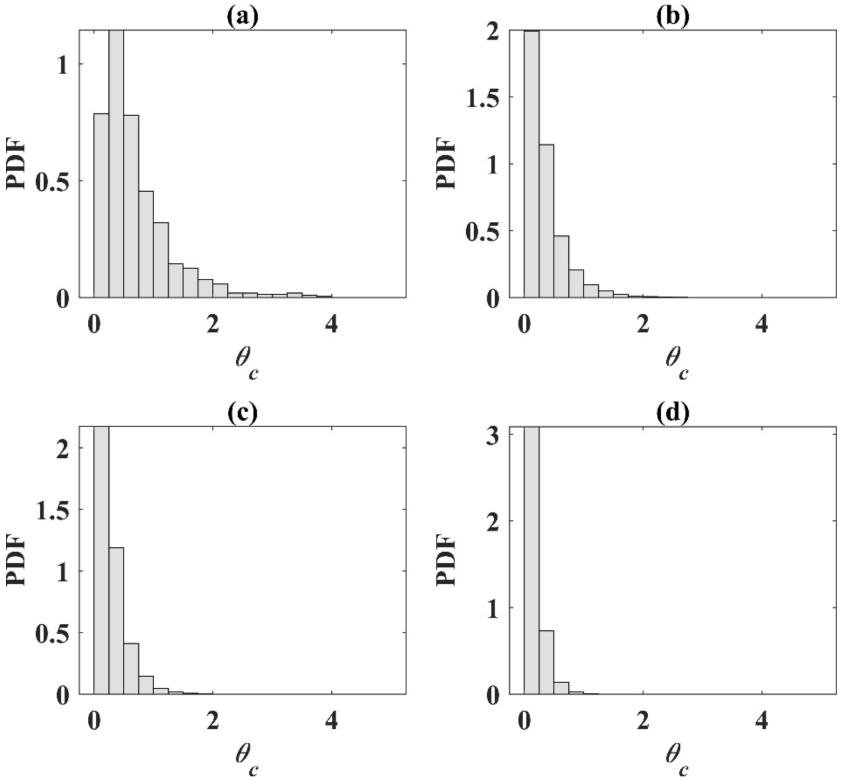

Figure 9. PDF of bubble collision angles in different regions of the channel in downflow at $Re_\tau = 150$ with $d_b = 110$ μm. (a) Viscous sublayer; (b) buffer layer; (c) log-law region; (d) bulk flow region.

Similar to the predictions of **Figs. 8** and **9**, the results for bubble collision velocities and collision angles in upflow are presented in **Figs. 10** and **11**, again confirming the generally low values of velocities and angles at which collisions occur, with the largest values of both again being found in the viscous sublayer. Due to the larger number of bubbles in the near-wall region in this case due to the influence of the lift force, and the higher turbulence levels and larger mean velocity gradients induced by bubbles moving faster in upflow than in downflow, the relative velocities and angles in the viscous sublayer are larger than in downflow, with collision angles up to 15 degrees observed. That said, collision velocities and angles are still generally small, confirming bubble collisions again happen on nearly rectilinear paths and with streamwise-only relative velocities.

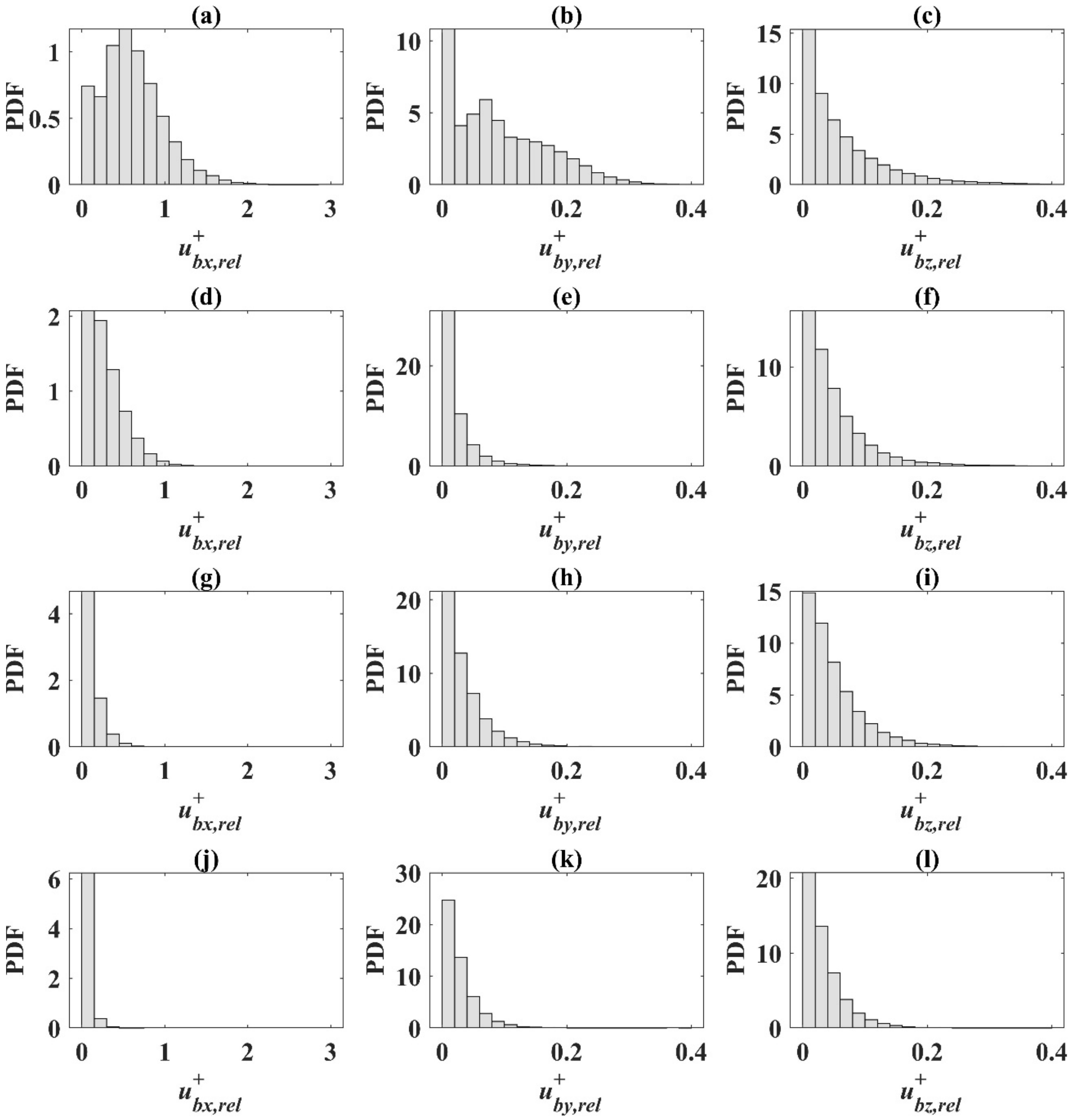

Figure 10. PDF of relative bubble collision velocities in the streamwise (*x*), wall-normal (*y*) and spanwise (*z*) directions in different regions of the channel in upflow at $Re_\tau = 150$ with d_b = 110 μm. (a), (b), (c) Viscous sublayer; (d), (e), (f) buffer layer; (g), (h), (i) log-law region; (j), (k), (l) bulk flow region.

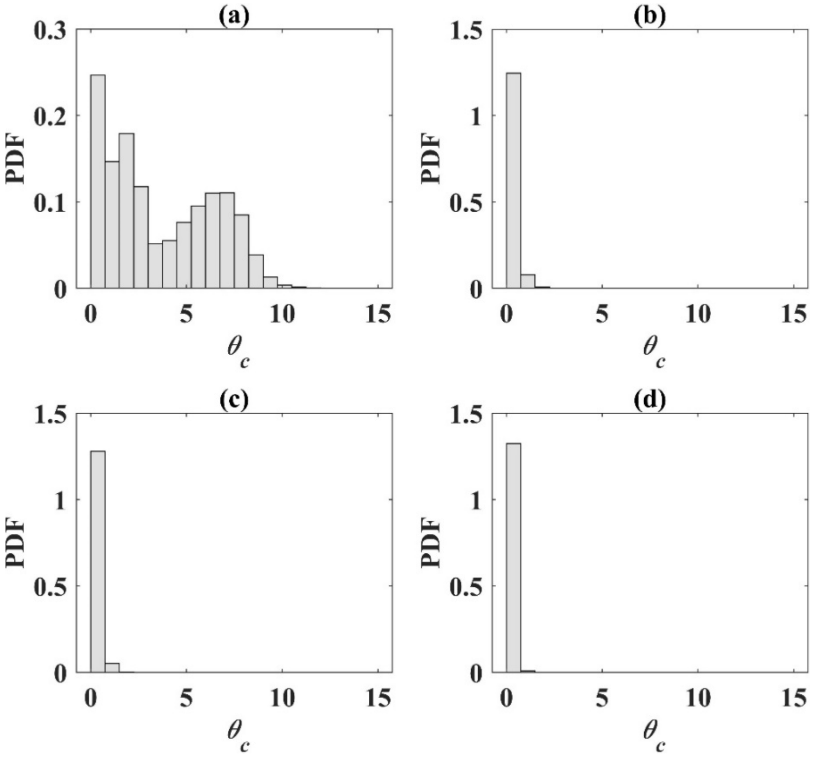

Figure 11. PDF of bubble collision angles in different regions of the channel in upflow at Re_τ = 150 with d_b = 110 μm. (a) Viscous sublayer; (b) buffer layer; (c) log-law region; (d) bulk flow region.

3.3 Four-way coupled flows with d_b = 330 μm bubbles

To further understand bubble collision dynamics, the bubble size effect was also considered. A total of 71,426 microbubbles with a larger diameter d_b = 330 μm, again corresponding to a void fraction of 0.1 %, were injected in the channel flow. Results for the upward and downward flows in terms of bubble velocity statistics and number density profiles were qualitatively similar to those given above for the smaller bubble diameter case, so are not reproduced here. Likewise, bubble collision velocities and angles in the four regions of the flow were again qualitatively similar. Because of this, comparison between results for the two bubble sizes is presented for the two regions of the flow that exhibited the greatest differences, namely the buffer layer in downflow and the viscous sublayer in upflow. PDFs for these cases are presented and compared in **Figs. 12** and **13**, respectively.

Overall, relative collision velocities and collision angles remain small in both regions of the flow, which confirms that, for the microbubbles considered, both bubble sizes tend to move and collide in nearly rectilinear paths. The results of **Fig. 12** for the buffer layer in downflow show that, for the larger microbubbles, the range of both bubble velocities and collision angles tends to be slightly larger than in the case of the 110 μm bubbles. The cause of this is worthy of further consideration, since shorter ranges might have been expected given that the larger inertia of 330 μm bubbles should make them less prone to be affected by the fluid flow. However, different phenomena may be responsible for the larger ranges, such as the higher shear across the bubble, and hence lift force, instantaneously experienced by the 330 μm bubbles in the most turbulent region of the flow. At the same time, as soon as coalescence begins, larger more buoyant bubbles are formed. The increase in bubble size with coalescence, and the corresponding difference in velocity, can be expected to be much larger for coalescing 330 μm bubbles than for 110 μm bubbles. These bubble size broadening effects would cause the 110 μm bubbles to have smaller relative streamwise velocities and collision angles, with peak probability values at lower levels.

In contrast, in **Fig. 13** for the viscous sublayer region in upflow, a generally similar range of relative velocity and collision angle magnitudes is found for both bubble sizes. Qualitative differences in the PDFs are, however, in general apparent. In particular, coalescence leading to larger bubble sizes was found to give rise to the accumulation of large coalesced 330 μm bubbles in the laminar viscous sublayer, again with much larger sizes than for the 110 μm case. These large bubbles remained close to the wall, decreasing through buoyancy effects the streamwise relative velocity and collision angle, and also shifting the probability distributions to lower values.

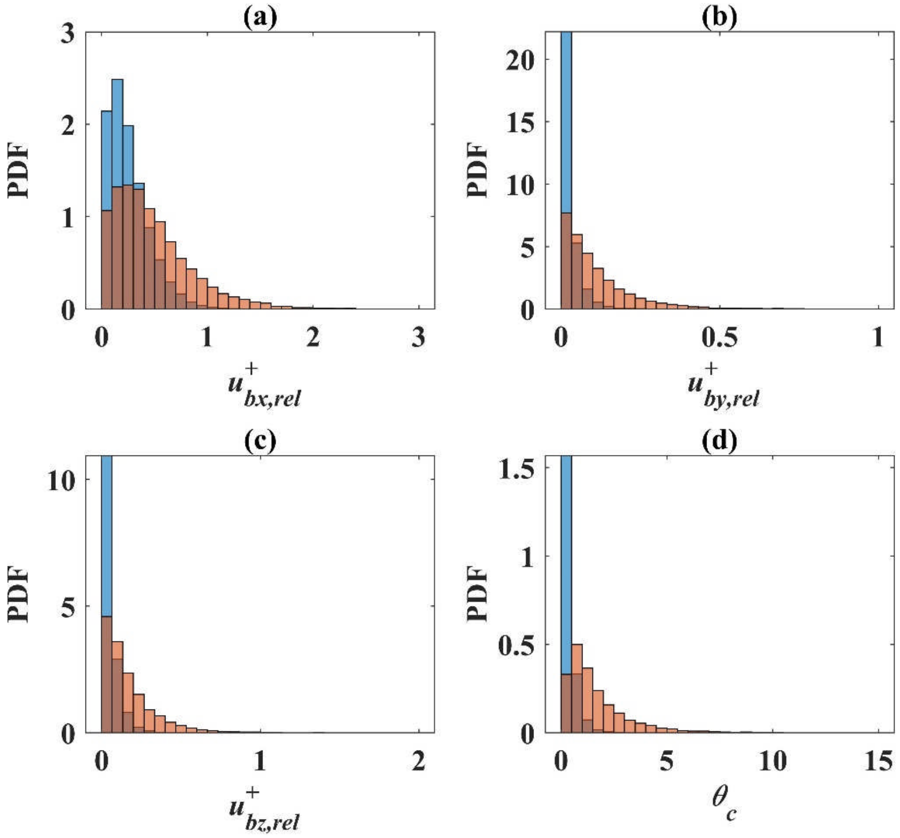

Figure 12. Comparison of PDFs of relative bubble collision velocities and angles in the buffer layer of the channel in downflow at $Re_\tau = 150$. (a), (b), (c) Collision velocities in the streamwise (x), wall-normal (y) and spanwise (z) directions; (d) collision angles (■ d_b = 330 μm; ■ d_b = 110 μm).

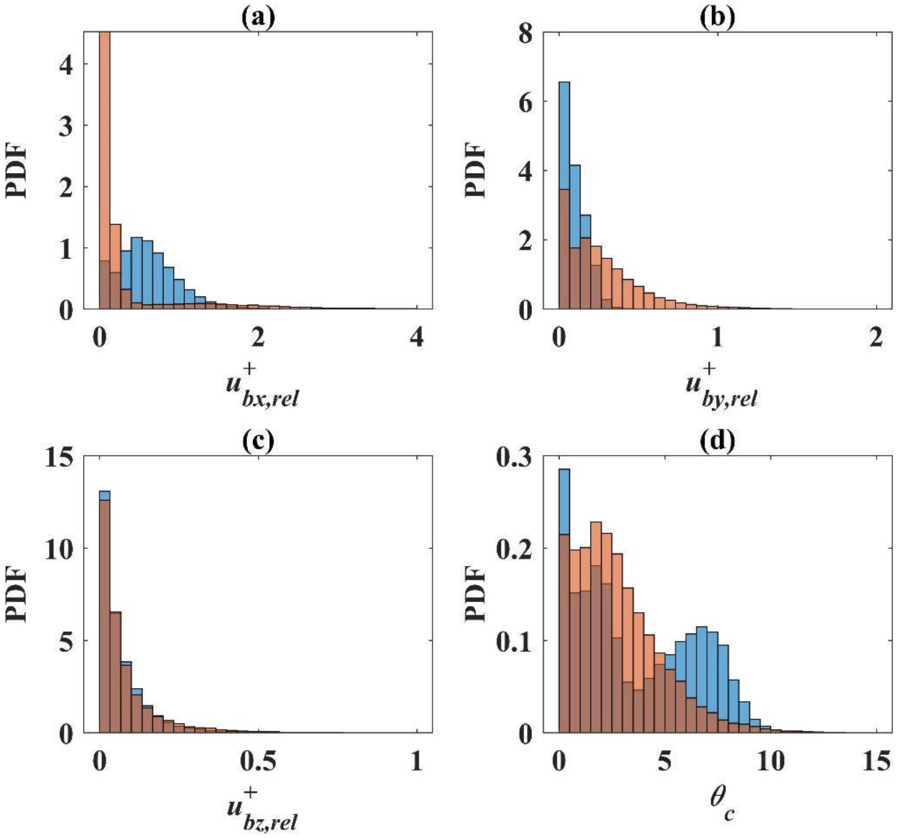

Figure 13. Comparison of PDFs of relative bubble collision velocities and angles in the viscous sublayer of the channel in upflow at $Re_\tau = 150$. (a), (b), (c) Collision velocities in the streamwise (x), wall-normal (y) and spanwise (z) directions; (d) collision angles (■ d_b = 330 μm; ■ d_b = 110 μm).

3.4 Bubble coalescence efficiency analysis

The distribution of recorded collision and coalescence events in the wall-normal direction predicted using the film drainage model is presented in **Fig. 14**. In upflow, because of the migration of bubbles towards the channel walls and the resulting high concentration of bubbles in that region, more collisions are found in the immediate vicinity of the wall than in the channel centre, as shown in **Fig. 14(a)**. The same is true, even if less markedly, in downflow, despite the migration of bubbles towards the channel centre due to the lift force. This occurs since, even if the concentration of bubbles is low near the wall, the near-wall region remains the area of the channel flow with the highest levels of turbulence and the largest velocity gradients, both of which promote collisions. However, in contrast with the upflow case, the number of collisions in downflow decreases in the very near-wall region (**Fig. 14(b)**) because of the very small number of bubbles that are found there. Similar results were obtained for the 330 μm bubbles.

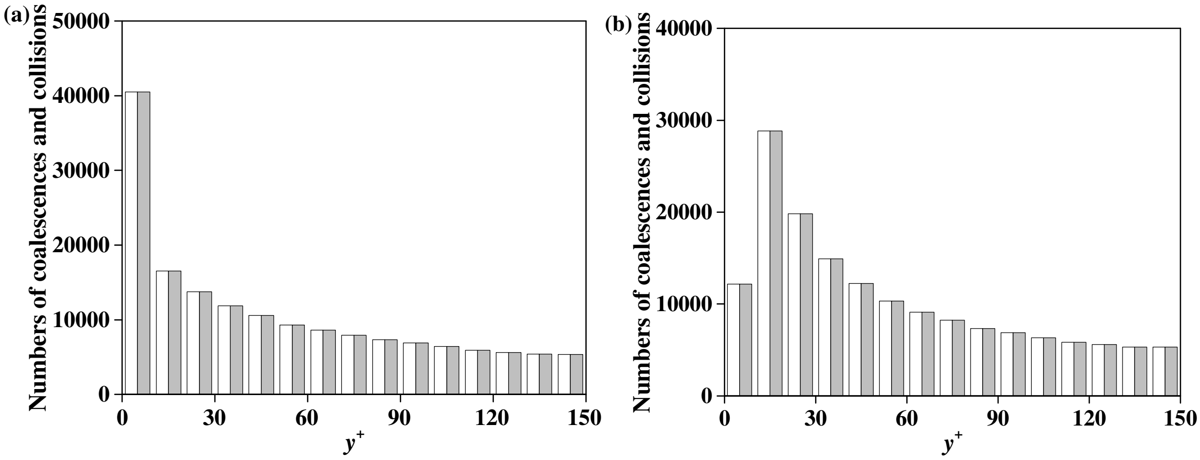

Figure. 14 Number of bubble collisions (□) and coalescences (■) in the wall-normal direction in (a) upflow and (b) downflow at $Re_\tau = 150$ with $d_b = 110$ µm.

In the results of **Fig. 14**, the coalescence efficiency is always found to be 100%, such that every collision in the channel results in a coalescence. These results were obtained using the model of Sommerfeld et al. [45], which estimates the bubble contact time from the time taken by a bubble with a certain relative collision velocity to travel a distance equal to a specified fraction of the bubble radius. This fraction is arbitrarily set to 0.25, and deceleration of the bubble during the collision process is neglected. For further verification, the contact time model of Kamp et al. [46] was also tested. The results, however, also showed the same 100% efficiency in both flows, with the contact time between the bubbles being always sufficient to allow drainage of the liquid film trapped between them. In contrast, additional results obtained with the energy model showed totally opposite behaviour, and a 0% coalescence efficiency was found for both flows. This suggests further development of more realistic coalescence models is desirable in future works.

An explanation for the 100% efficiency of the film drainage model, and 0% for the energy model, can be found in the results of **Figs. 8** to **11**. Due to the small bubble relative velocities and collision angles, nearly rectilinear collisions are predicted to occur. As a consequence of the type of collision, the predicted contact time is always high, which explains the 100% efficiency returned by the film drainage model. Conversely, according to the energy model of Sovová [47], a high critical bubble velocity is required to give rapid coalescence, otherwise coalescence is unlikely. Therefore, given the low relative velocity observed, which implies low-energy collisions, the 0% efficiency returned by the energy model is not entirely surprising.

Asiagbe et al. [56] employed large eddy simulation (LES) to examine air bubble collision and coalescence in water flows at $Re_\tau = 150$ with $d_b = 220$ μm bubbles using a similar film drainage coalescence model. In evaluating coalescence efficiency, the authors observed that, in the near-wall region, the bubbles experience shorter contact times. In these regions, this resulted in not all collisions leading to coalescence in both upward and downward flows, although towards the centre of the channel, where turbulence levels are lower, 100% or near-100% coalescence efficiency was achieved. Nevertheless, collisions efficiencies were always high (> 95%), even in the near-wall region, apart from in the upflow case where the efficiency was significantly reduced. Similarly, Asiagbe et al. [36], in considering a $Re_\tau = 150$ horizontal channel flow with $d_b = 110$ μm bubbles, observed an effectively 100% coalescence efficiency throughout the flow, with this attributed to the low flow Reynolds number. The work of Asiagbe et al. [36,56] used a high resolution LES with 2.1 M nodes although, clearly, not all the velocity scales were resolved, with the smallest scaled modelled after filtering. The unresolved scales, particularly near the wall, will have some effect on the bubble motion, and may be responsible for the differences found between the DNS- and LES-based simulations. Nevertheless, the differences between results based on the two simulation approaches are relatively small, particularly in view of the 100% efficiency returned by the film drainage model, and the 0% by the energy model, in the present work. As noted, therefore, further assessment of existing coalescence models, and the development of more realistic models, is required for use in Lagrangian bubble tracking approaches.

4 Summary and Conclusions

Turbulent upward and downward flows of microbubbles in a channel were studied using a four-way coupled Eulerian-Lagrangian approach. The accuracy of the model was successfully verified by comparison with single-phase and two-way coupled results available in the literature. The four-way coupled model provided a quantitative description of the microbubble flows and highlighted the mechanisms responsible for bubble collision and coalescence, driven by the continuous phase fluid flow. At the levels of turbulence investigated, collisions mainly occur on quasi-rectilinear bubble trajectories. Therefore, the angle of collision is usually very small and the relative approach velocity between the two colliding bubbles is generally low. These low-energy collisions favour use of the film drainage coalescence model over the energy model, but the contradictory predictions obtained from these two approaches is in need of further investigation. The development of more accurate and generally applicable coalescence models, possibly extended to cover recently observed behaviours specific to small microbubbles, such as clouding in vortices and low-speed streaks, will be pursued. The understanding generated on the dynamics of bubble-bubble interactions, which at the level of turbulence employed mainly occur on nearly rectilinear patterns, is of value to the further development of such models, and the closure relations used in macroscopic Eulerian-Eulerian approaches.

Acknowledgments

JZ gratefully acknowledges funding through an Anniversary Research Scholarship from the University of Leeds.

Compliance with Ethical Standards

Conflict of interests The authors declare that they have no conflict of interest.

References

1. Balachandar, S., Eaton, J.K.: Turbulent dispersed multiphase flow. Annu. Rev. Fluid Mech. **42**, 111-133 (2010)

2. Todreas, N.E., Kazimi, M.S.: Nuclear systems volume I: Thermal hydraulic fundamentals. CRC press, Boca Raton (2011)

3. Shah, Y.T., Kelkar, B.G., Godbole, S.P., Deckwer, W.D.: Design parameters estimations for bubble column reactors. AIChE J. **28**, 353-379 (1982)

4. Lau, Y.M., Deen, N.G., Kuipers, J.A.M.: Development of an image measurement technique for size distribution in dense bubbly flows. Chem. Eng. Sci. **94**, 20-29 (2013)

5. Elghobashi, S.: On predicting particle-laden turbulent flows. Appl. Sci. Res. **52**, 309-329 (1994)

6. Deen, N.G., van Sint Annaland, M., Kuipers, J.A.M.: Multi-scale modeling of dispersed gas–liquid two-phase flow. Chem. Eng. Sci. **59**, 1853-1861 (2004)

7. Rasquin, M., Smith, C., Chitale, K., Seol, E.S., Matthews, B.A., Martin, J.L., Sahni, O., Loy, R.M., Shephard, M.S., Jansen, K.E.: Scalable implicit flow solver for realistic wing simulations with flow control. Comput. Sci. Eng. **16**, 13-21 (2014)

8. Kuerten, J.G.M.: Point-particle DNS and LES of particle-laden turbulent flow - a state-of-the-art review. Flow Turbul. Combust. **97**, 689-713 (2016)

9. Wang, L.-P., Maxey, M.R.: The motion of microbubbles in a forced isotropic and homogeneous turbulence. Appl. Sci. Res. **51**, 291-296 (1993)

10. Spelt, P.D.M., Biesheuvel, A.: On the motion of gas bubbles in homogeneous isotropic turbulence. J. Fluid Mech. **336**, 221-244 (1997)

11. Mazzitelli, I.M., Lohse, D., Toschi, F.: On the relevance of the lift force in bubbly turbulence. J. Fluid Mech. **488**, 283-313 (2003)

12. Snyder, M.R., Knio, O.M., Katz, J., Le Maître, O.P.: Statistical analysis of small bubble dynamics in isotropic turbulence. Phys. Fluids **19**, 065108 (2007)

13. Mazzitelli, I.M., Lohse, D., Toschi, F.: The effect of microbubbles on developed turbulence. Phys. Fluids **15**, L5-L8 (2003)

14. Wen, L.H., Ismail, A.B., Menon, P.M., Saththasivam, J., Thu, K., Choon, N.K.: Case studies of microbubbles in wastewater treatment. Desalin. Water Treat. **30**, 10-16 (2011)

15. Ferrante, A., Elghobashi, S.: Reynolds number effect on drag reduction in a microbubble-laden spatially developing turbulent boundary layer. J. Fluid Mech. **543**, 93-106 (2005)

16. Maxey, M.R., Chang, E.J., Wang, L.P.: Simulation of interactions between microbubbles and turbulent Flows. App. Mech. Rev. **47**, S70-S74 (1994)

17. Molin, D., Marchioli, C., Soldati, A.: Turbulence modulation and microbubble dynamics in vertical channel flow. Int. J. Multiphas. Flow **42**, 80-95 (2012)

18. Deutsch, S., Castano, J.: Microbubble skin friction reduction on an axisymmetric body. Phys. Fluids **29**, 3590-3597 (1986)

19. Madavan, N.K., Deutsch, S., Merkle, C.L.: Reduction of turbulent skin friction by microbubbles. Phys. Fluids **27**, 356-363 (1984)

20. Pal, S., Merkle, C.L., Deutsch, S.: Bubble characteristics and trajectories in a microbubble boundary layer. Phys. Fluids **31**, 744-751 (1988)

21. Ferrante, A., Elghobashi, S.: On the physical mechanisms of drag reduction in a spatially developing turbulent boundary layer laden with microbubbles. J. Fluid Mech. **503**, 345-355 (2004)

22. Giusti, A., Lucci, F., Soldati, A.: Influence of the lift force in direct numerical simulation of upward/downward turbulent channel flow laden with surfactant contaminated microbubbles. Chem. Eng. Sci. **60**, 6176-6187 (2005)

23. Lu, J., Corvalan, C.M., Chew, Y.M.J., Huang, J.-Y.: Coalescence of small bubbles with surfactants. Chem. Eng. Sci. **196**, 493-500 (2019)

24. Gutiérrez-Torres, C.C., Hassan, Y.A., Jimenez-Bernal, J.A.: Turbulence structure modification and drag reduction by microbubble injections in a boundary layer channel flow. J. Fluids Eng. **130**, 111304 (2008)

25. Park, H.J., Saito, D., Tasaka, Y., Murai, Y.: Color-coded visualization of microbubble clouds interacting with eddies in a spatially developing turbulent boundary layer. Exp. Therm. Fluid Sci. **109**, 109919 (2019)

26. Yonemoto, Y., Yanagisawa, H., Kawara, Z., Kunugi, T.: Coalescence of microbubble. J. JSEM. **8**, 38-44 (2008)

27. Jacob, B., Olivieri, A., Miozzi, M., Campana, E.F., Piva, R.: Drag reduction by microbubbles in a turbulent boundary layer. Phys. Fluids **22**, 115104 (2010)

28. Liao, Y., Lucas, D.: A literature review on mechanisms and models for the coalescence process of fluid particles. Chem. Eng. Sci. **65**, 2851-2864 (2010)

29. Shinnar, R., Church, J.M.: Statistical theories of turbulence in predicting particle size in agitated dispersions. Ind. Eng. Chem. Res. **52**, 253-256 (1960)

30. Shinnar, R.: On the behaviour of liquid dispersions in mixing vessels. J. Fluid Mech. **10**, 259-275 (1961)

31. Howarth, W.J.: Coalescence of drops in a turbulent flow field. Chem. Eng. Sci. **19**, 33-38 (1964)

32. Lehr, F., Millies, M., Mewes, D.: Bubble-size distributions and flow fields in bubble columns. AlChE J. **48**, 2426-2443 (2002)

33. Hoppe, F., Breuer, M.: A deterministic and viable coalescence model for Euler-Lagrange simulations of turbulent microbubble-laden flows. Int. J. Multiphas. Flow **99**, 213-230 (2018)

34. Chen, R., Yu, H., Zhu, L., Patil, R.M., Lee, T.: Spatial and temporal scaling of unequal microbubble coalescence. AIChE J. **63**, 1441-1450 (2017)

35. Takagi, S., Matsumoto, Y.: Surfactant effects on bubble motion and bubbly flows. Annu. Rev. Fluid Mech. **43**, 615-636 (2011)

36. Asiagbe, K.S., Fairweather, M., Njobuenwu, D.O., Colombo, M.: Large eddy simulation of microbubble transport in a turbulent horizontal channel flow. Int. J. Multiphase. Flow **94**, 80-93 (2017)

37. Asiagbe, K.S., Fairweather, M., Njobuenwu, D.O., Colombo, M.: Large eddy simulation of microbubble dispersion and flow field modulation in vertical channel flows. AIChE J. **65**, 1325-1339 (2019)

38. Fischer, P., Kruse, J., Mullen, J., Tufo, H., Lottes, J., Kerkemeier, S.: Nek5000: Open source spectral element CFD solver. https://nek5000.mcs.anl.gov (2008)

39. Patera, A.T.: A spectral element method for fluid dynamics: Laminar flow in a channel expansion. J. Comput. Phys. **54**, 468-488 (1984)

40. Naumann, Z., Schiller, L.: A drag coefficient correlation. Z Ver Deutsch Ing **77**, 318-323 (1935)

41. Brennen, C.E.: A review of added mass and fluid inertial forces. Naval Civil Engineering Laboratory, Port Hueneme, California, (1982)

42. Maxey, M.R., Riley, J.J.: Equation of motion for a small rigid sphere in a nonuniform flow. Phys. Fluids **26**, 883-889 (1983)

43. Legendre, D., Magnaudet, J.: The lift force on a spherical bubble in a viscous linear shear flow. J. Fluid Mech. **368**, 81-126 (1998)

44. Prince, M.J., Blanch, H.W.: Bubble coalescence and break-up in air-sparged bubble columns. AlChE J. **36**, 1485-1499 (1990)

45. Sommerfeld, M., Bourloutski, E., Bröder, D.: Euler/Lagrange calculations of bubbly flows with consideration of bubble coalescence. Can. J. Chem. Eng. **81**, 508-518 (2003)

46. Kamp, A.M., Chesters, A.K., Colin, C., Fabre, J.: Bubble coalescence in turbulent flows: A mechanistic model for turbulence-induced coalescence applied to microgravity bubbly pipe flow. Int. J. Multiphase. Flow **27**, 1363-1396 (2001)

47. Sovová, H.: Breakage and coalescence of drops in a batch stirred vessel—II comparison of model and experiments. Chem. Eng. Sci. **36**, 1567-1573 (1981)

48. Chesters, A.K.: Modelling of coalescence processes in fluid-liquid dispersions: a review of current understanding. Chem. Eng. Res. Des. **69**, 259-270 (1991)

49. Oolman, T.O., Blanch, H.W.: Bubble coalescence in stagnant liquids. Chem. Eng. Commun. **43**, 237-261 (1986)

50. Lu, J., Biswas, S., Tryggvason, G.: A DNS study of laminar bubbly flows in a vertical channel. Int. J. Multiphas. Flow **32**, 643-660 (2006)

51. Tryggvason, G., Ma, M., Lu, J.: DNS–Assisted modeling of bubbly flows in vertical channels. Nucl. Sci. Eng. **184**, 312-320 (2016)

52. Bolotnov, I.A., Jansen, K.E., Drew, D.A., Oberai, A.A., Lahey, R.T., Podowski, M.Z.: Detached direct numerical simulations of turbulent two-phase bubbly channel flow. Int. J. Multiphase. Flow **37**, 647-659 (2011)

53. Clift, R., Grace, J.R., Weber, M.E.: Bubbles, drops, and particles. vol. Book, Whole. Academic Press, London;New York; (1978)

54. Tomiyama, A., Tamai, H., Zun, I., Hosokawa, S.: Transverse migration of single bubbles in simple shear flows. Chem. Eng. Sci. **57**, 1849-1858 (2002)

55. Liu, N., Cheng, B., Que, X., Lu, X.: Direct numerical simulations of turbulent channel flows with consideration of the buoyancy effect of the bubble phase. J. Hydrodyn. **23**, 282-288 (2011)

56. Asiagbe, K.S., Fairweather, M., Njobuenwu, D.O., Colombo, M.: Microbubbles coalescence during transport in vertical channel flows. In: Friedl, A., Klemeš, J.J., Radl, S., Varbanov, P.S., Wallek, T. (Eds.) Computer Aided Chemical Engineering, Vol. 43. pp. 79-84. Elsevier, (2018)